IEICE TRANS. INF. & SYST., VOL.E94–D, NO.4 APRIL 2011

PAPER

Parameter Estimation for Non-convex Target Object Using Networked Binary Sensors*

Hiroshi SAITO[†a)], ***Fellow***, **Sadaharu TANAKA**[††], ***Nonmember***, ***and*** **Shigeo SHIODA**[††], ***Member***

SUMMARY We describe a parameter estimation method for a target object in an area that sensors monitor. The parameters to be estimated are the perimeter length, size, and parameter determined by the interior angles of the target object. The estimation method does not use sensor location information, only the binary information on whether each sensor detects the target object. First, the sensing area of each sensor is assumed to be line-segment-shaped, which is a model of an infrared distance measurement sensor. Second, based on the analytical results of assuming line-segment-shaped sensing areas, we developed a unified equation that works with general sensing areas and general target-object shapes to estimate the parameters of the target objects. Numerical examples using computer simulation show that our method yields accurate results.

key words: *parameter estimation, shape estimation, sensor network, ubiquitous network, integral geometry*

1. Introduction

Recent developments in electronics and micromechanics have enabled the fabrication of small, low-cost, low-power sensor nodes that have communication capabilities and built-in batteries. Such sensor nodes communicating via a wireless link for transmitting sensory data on detected events of interest can be used to build wireless sensor networks [1]–[3].

In most previous developments, sensor networks have used ad hoc multi-hop network technologies. In these sensor networks, sensor nodes require CPU computing power to calculate routes and handle complicated protocols, and wireless links require enough bandwidth to transmit routing protocol messages. Consequently, they consume a non-negligible amount of battery life. This implies that sensor nodes are similar to personal computers, which are normally expensive and offer high performance, and that wireless links connecting sensor nodes typically use a wireless LAN, which is normally high-speed, short or medium range. This network is suitable for sensor networks that have a limited number of sensor nodes with advanced functions and high performance. The sensor nodes are placed in accordance with a careful design or may have GPS functions.

In contrast, use of a newly proposed network such as Wide Area Ubiquitous Network [4] may open up a new sensing paradigm, because this network is similar to cellular phone network architecture, supports terminals with low performance and functionalities, and has a long-range, low-speed wireless link with very low power consumption. That is, instead of having a few sensors with advanced functions and high performance, many sensors with simple functions and low performance are distributed randomly. They are networked and send reports, each of which includes only a small amount of information, over a low-speed wireless link. However, from the network as a whole, we can extract a significant amount of information.

Considering such sensor networks, we studied a method for estimating parameters (the perimeter length, the size, and a parameter determined by the interior angles of the target object) of a target object by using networked binary sensors whose locations are unknown. An individual sensor is simple. It monitors its environment and reports whether it detects the target object. It does not have a positioning function, such as a GPS, nor does it monitor the size and shape of the target object, such as with a camera. In addition, its placement is not carefully designed. By collecting reports from individual sensors, we can statistically estimate parameters related to the size and shape of the target object. The possibility of estimating parameters related to the size and shape through the use of binary data sensed at unknown locations is not intuitive.

This research is an extension of our prior studies. Reference [5] is based on the coverage process theory [6] and its application to sensor networks [7]–[9]. In [5], sensors that measure the size of a detected part of the target object are used for estimating the overall size. For estimating a parameter related to its shape, the shape category (such as rectangular or doughnut-shaped) of the target object must be known a priori to calculate the object's detectable area. We removed such problems and developed an estimation method for parameters related to the shape and size of the target object using binary sensors that send reports on whether they detect the target object [10]. That study mainly focused on the cases in which both the target object and the sensing area are convex and the sensing area is disk-shaped. The developed method was evaluated through an experiment where the target object was a box and the sensor was an infrared distance measurement sensor [11]. The experimental results showed that our theoretical results are valid, although we need some assumptions to derive those theoretical results. However, we have not obtained a theory applicable to the estimation of non-convex target objects when we use

Manuscript received March 19, 2010.
Manuscript revised November 29, 2010.

[†]The author is with NTT Service Integration Laboratories, NTT Corporation, Musashino-shi, 180–8585 Japan.
[††]The authors are with Chiba University, Chiba-shi, 263–8522 Japan.

*Parts of this paper were presented at IEEE SUTC 2010.

a) E-mail: saito.hiroshi@lab.ntt.co.jp

DOI: 10.1587/transinf.E94.D.772

such an infrared distance measurement sensor. We now extend the previous method to a more general method applicable even to non-convex target objects when an infrared distance measurement sensor is used. Our new method enables the practical estimation of both a convex and a non-convex target object by using sensors for which the sensing areas are line-segment-shaped. Furthermore, we extend this method to estimate both a convex and a non-convex target object by using sensors for which the sensing areas are of any shape.

The rest of this paper is organized as follows. Section 2 describes the model used in this work and summarizes the past results. Section 3 presents the analytical results for the detectable area of the target object. Section 4 describes the estimation method developed on the basis of the results in the previous section. Section 5 gives numerical examples using computer simulations to verify our new estimation method. Section 6 presents the conclusion.

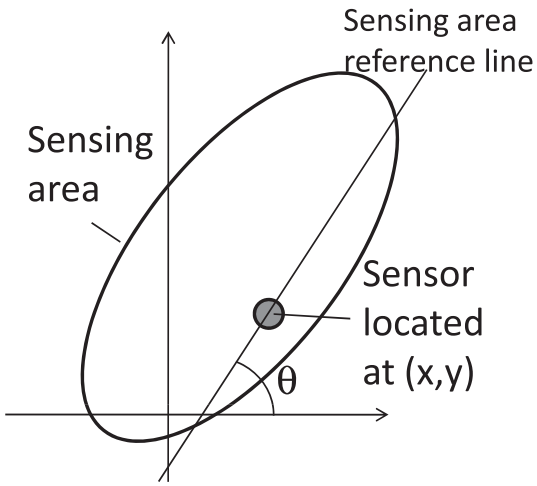

Fig. 1 Sensing area.

2. Model

Assume that a target object $\mathcal{T}$ exists in 2-dimensional space $\mathbb{R}^2$. Its size is $\|\mathcal{T}\|$ and its perimeter length is $|\mathcal{T}|$, where $\|x\|$ denotes the size of x and $|x|$ denotes the perimeter length of x. The location of the target object is unknown.

To determine the size $\|\mathcal{T}\|$, the perimeter length $|\mathcal{T}|$, and a parameter related to the shape of the target object $\mathcal{T}$, a sensor network operator deploys sensors in 2-dimensional space without knowing their resulting locations. The sensors are networked, and the mean density of these sensors is λ. Each sensor has a sensing area, and it monitors the environment and detects events within that area. Therefore, if and only if the target object is in that area, will the sensor detect the target object. This model is called the Boolean sensing model [8], [12]–[14] because whether a point is sensed is clearly distinguished.

Assume that a sensor is located at (x, y) and the sensing area reference line, which is an arbitrary line attached to the sensing area and is rotated if the sensing area is rotated, is rotated by θ from the referenced position. Denote its sensing area as $\mathcal{A}(x, y, \theta) \subset \mathbb{R}^2$ (Fig. 1). Each sensor can communicate with the sensor operation center and send a report indicating whether or not the sensor detects the target object. That is, the report is $\mathbf{1}(\mathcal{A}(x, y, \theta) \cap \mathcal{T} \neq \emptyset)$, where $\mathbf{1}(\omega)$ is an indicator function that becomes 1 if a statement ω is true and 0 if otherwise. The sensor network operator receives the report from each sensor through the network.

Assume that if and only if a sensor of which sensing area is $\mathcal{A}$ is located in a detectable area $\mathcal{D}(\mathcal{T}, \mathcal{A}) \subset \mathbb{R}^3$ of the target object does it detect the target object. That is, $\mathbf{1}(\mathcal{A}(x, y, \theta) \cap \mathcal{T} \neq \emptyset) = 1$ if and only if $(x, y, \theta) \in \mathcal{D}(\mathcal{T}, \mathcal{A})$. Equivalently, $\mathcal{D} = \{(x, y, \theta) | \mathcal{A}(x, y, \theta) \cap \mathcal{T} \neq \emptyset\}$. In the rest of this paper, we analyze the detectable area $\mathcal{D}$ and its size $\|\mathcal{D}\| = \frac{1}{2\pi} \int_{\mathcal{D}} dxdyd\theta$. The objective of this analysis is to show that $\|\mathcal{D}\|$ can be described by the linear combination of the size, the perimeter length, and a parameter(s) related to the shape of the target object.

For a convex target object, we have obtained the following equation and developed an estimation method for its perimeter length $|\mathcal{T}|$ and size $\|\mathcal{T}\|$, where the sensing area $\mathcal{A}$ is also convex [10].

$$\|\mathcal{D}\| = \frac{1}{2\pi} |\mathcal{T}| \cdot |\mathcal{A}| + \|\mathcal{T}\| + \|\mathcal{A}\|. \quad (1)$$

However, for target objects that are not convex, there has been no equation applicable to all cases, and an estimation method has not been thoroughly explored. To the best of the authors' knowledge, the only result pertaining to non-convex targets is from our previous research [10]. In that paper, we conjectured an equation for the case of disk-shaped sensing areas and for a certain class of non-convex target objects.

Due to this, we have not been able to implement the estimation method for non-convex target objects through sensors using, for example, lasers and infrared emitting diodes, as described in [11], because their narrow and sharp sensing areas cannot be modeled as a disk. Our current study focuses on parameters such as perimeter length and size estimation of non-convex target objects.

3. Analysis

This section gives a theoretical background of the estimation method proposed later. It can estimate parameters of r-tractable ($2r$-tractable) target objects. Roughly speaking, an r-tractable target object is one that does not have dents less-than-r wide. The formal definition of "r-tractable" is in the Appendix. Practically, many target objects are approximated by r-tractable ($2r$-tractable) target objects.

3.1 Line-Segment-Shaped Sensing Area

This subsection assumes that the sensing area of each sensor is a line segment of length r, which is a typical model of sensing areas of lasers and infrared emitting diodes. The size of the detectable area that is associated with the target

object and with the line-segment-shaped sensing area is presented. When the sensor of the line-segment-shaped sensing area is located at (x, y) with the rotation angle θ, the sensing area is a line segment from (x, y) to $(x + r\cos\theta, y + r\sin\theta)$, where $0 \le \theta < 2\pi$.

We can then obtain an equation for the size of the detectable area under the line-segment-shaped sensing area.

[Proposition for line-segment-shaped sensing areas]

Assume that the sensing area of each sensor is a line segment of length r. The target object $\mathcal{T}$ is r-tractable, and its boundary is a simple closed curve consisting of line segments. Then,

$$\|\mathcal{D}\| = \alpha r^2 + \frac{r}{\pi}|\mathcal{T}| + \|\mathcal{T}\|. \tag{2}$$

Here, $\alpha = \frac{1}{4\pi}\sum_i \mathbf{1}(\pi < \phi_i)\{-1+(-\pi+\phi_i)\cos\phi_i/\sin\phi_i\}$ where ϕ_i is the i-th interior angle of the target object.

Proof is shown in Appendix. A convex target object is r-tractable and $\alpha = 0$. Thus, Eq. (1) is a special case of Eq. (2) for line-segment-shaped sensing areas.

Applying similar discussions used for the exterior boundary to the interior boundary, we can extend this proposition to target objects containing holes. That is,

[Corollary for target object containing holes with line-segment-shaped sensing areas]

Assume that each (exterior or interior) boundary of the target object is a simple closed curve consisting of line segments. If all the line segments of the boundary are assumed to be r-tractable, Eq. (2) is valid.

For the disk-shaped holes, we obtain the following corollary. Note that a hole in a target object is not r-tractable.

[Corollary for target object containing disk-shaped holes with line-segment-shaped sensing areas]

Assume that the sensing area of each sensor is a line segment of length r. Consider a target object $\tilde{\mathcal{T}}$. Let $\tilde{\mathcal{D}}$ be its detectable area. Construct a new target object by making a disk-shaped hole of radius $a > r$. Then, the size of the detectable area $\mathcal{D}$ and the perimeter length and size of the new target object $\mathcal{T}$ are given as follows:

$$\|\mathcal{D}\| = \|\tilde{\mathcal{D}}\| - \left(2a^2\cos^{-1}\left(\frac{r}{2a}\right) - ar\sqrt{1-\left(\frac{r}{2a}\right)^2}\right), \tag{3}$$

$$|\mathcal{T}| = |\tilde{\mathcal{T}}| + 2\pi a, \tag{4}$$

and

$$\|\mathcal{T}\| = \|\tilde{\mathcal{T}}\| - \pi a^2. \tag{5}$$

The corollary mentioned above is given as follows. If there is a hole, the detectable area size reduces by the size of the intersection area made by two disks for which the radiuses are a and for which the centers are r apart (see Fig. 2). The size of the intersection is $2(a^2\cos^{-1}(\frac{r/2}{a}) - ar\sin(\cos^{-1}(\frac{r/2}{a})/2)$.

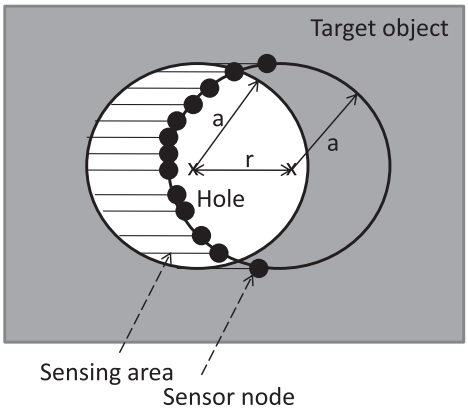

Fig. 2 Disk-shaped hole.

3.2 Disk-Shaped Sensing Areas

By using the concept "r-tractable," we can prove the following proposition, which has the same equation conjectured in [10], under assumptions different from those used in [10]. Proof is shown in the Appendix.

[Proposition for disk-shaped sensing areas]

Assume that the sensing area of each sensor is a disk of radius r. The target object $\mathcal{T}$ is $2r$-tractable, and its boundary is a simple closed curve consisting of line segments. Then,

$$\|\mathcal{D}\| = \alpha r^2 + r|\mathcal{T}| + \|\mathcal{T}\|. \tag{6}$$

Here, $\alpha = \sum_j\{\mathbf{1}(\phi_j < \pi)\frac{\pi-\phi_j}{2} + \mathbf{1}(\phi_j > \pi)\frac{1+\cos\phi_j}{\sin\phi_j}\}$.

[Corollary for target object containing holes with disk-shaped sensing areas]

Assume that each (exterior or interior) boundary of the target object is a simple closed curve consisting of line segments. If all the line segments of the boundary are assumed to be $2r$-tractable, Eq. (6) is valid.

For the disk-shaped sensing area and the target object with a disk-shaped hole, the detectable area size is given in [10].

3.3 Sensing Area of General Shape

For the line-segment-shaped sensing areas, Eq. (2) is valid. In addition, for disk-shaped sensing areas, Eq. (6) is valid. Therefore, we conjecture that a similar equation is valid for much broader classes of sensing areas than disk-shaped and line-segment-shaped ones. As a candidate for a unified equation including Eqs. (1), (2), and (6) as special cases, we propose the following.

[Unified equation for convex sensing areas]

Define $r = max_{\mathbf{x}_1,\mathbf{x}_2\in\mathcal{A}}|\mathbf{x}_1 - \mathbf{x}_2|$. The target object $\mathcal{T}$ is r-tractable, and its boundary is a simple closed curve consisting of line segments. Then,

$$\|\mathcal{D}\| = \|\mathcal{T}\| + \frac{1}{2\pi}|\mathcal{A}|\cdot|\mathcal{T}| + \beta_1|\mathcal{A}|^2 + \beta_2\|\mathcal{A}\|. \tag{7}$$

Here, $\beta_1 = \sum_i \alpha_i$, $\beta_2 = \frac{\sum_j(\pi-\phi_j)}{2\pi}$, ϕ_j is the j-th interior angle smaller than π, and α_i is a constant determined only by the i-th interior angle larger than π of the target objects.

Note that $\sum_j \phi_j = (n-2)\pi$ for the convex target object with n vertexes. Thus, Eq. (7) is identical to Eq. (1) for the convex target object. In addition, for the disk-shaped sensing area for which the radius is r, $|\mathcal{A}| = 2\pi r$ and $\|\mathcal{A}\| = \pi r^2$. Therefore, Eq. (7) is identical to Eq. (6) for the disk-shaped sensing area. Furthermore, for the line-segment-shaped sensing area for which length is r, $|\mathcal{A}| = 2r$ and $\|\mathcal{A}\| = 0$. Therefore, Eq. (7) is identical to Eq. (2) for the line-segment-shaped sensing area. The validity of this equation is checked through numerical examples shown later in this paper.

4. Estimation Methods

The analytical results in the previous section enable us to estimate the parameters of a target object by using the report from a binary sensor, even if there is no sensor location information. The essence of this estimation method is based on the following three points: (1) the expected number of sensors detecting the target object is $\lambda\|\mathcal{D}\|$, where λ is the mean sensor density; (2) the sample value of this number is the number of reports detecting the target object; and (3) the size and perimeter length of the target object and a parameter α (parameters β_1 and β_2) are expressed as a function of the detectable area size and the sensing area parameters.

We introduce three (four) types of sensors that have different sensing-area perimeter lengths for estimating the unknown parameters, size, and perimeter length of the target object, and a parameter α (parameters β_1 and β_2). By applying the three steps mentioned above, we can obtain a set of least square error estimators for unknown parameters. In the following subsection, we describe this in more detail. When we emphasize the fact that $\mathcal{D}$ is a function of a sensing area radius r, $\mathcal{D}(r)$ is used.

4.1 Additional Notation

Assume that the target object moves. (This assumption is not essential. If the target object does not move, we use the sensory data at a single time instant.) At $t = t_k$, the i-th sensor sends a report, $I_i(t_k)$, describing whether it detects the target object.

Multiple sensor types that have different perimeters of sensing areas are introduced. Let λ_j be the mean density of type-j sensors. Assume that the $n_{j-1}+1, \cdots, n_j$-th sensors are type-j sensors and $n_0 = 0$. $\tilde{I}_j(t_k) = \sum_{i=n_{j-1}+1}^{n_j} I_i(t_k)$ denotes the number of type-j sensors detecting the target object at t_k, and $\bar{I}_j = \sum_{k=1}^{m} I_j(t_k)/m$ denotes its time average. We assume that the sensor network operator knows the sensor type of each sensor sending a report.

4.2 Estimation

In this subsection, we introduce three types of sensors and assume that the sensing area of the type-j sensors is line-segment-shaped with length r_j (disk-shaped with radius r_j).

We use $\tilde{I}_j(t_k)$ as an estimator of $\lambda_j\|\mathcal{D}(r_j)\|$ for $j = 1, 2, 3$ and apply Eq. (2) (Eq. (6)). Note that $\lambda_j\|\mathcal{D}(r_j)\| = E[\tilde{I}_j(t_k)]$. Thus, Eq. (2) or (6) can be rewritten as

$$\tilde{I}_j(t_k) = \lambda_j\left(\alpha r_j^2 + \frac{|\mathcal{A}_j|}{2\pi}|\mathcal{T}| + \|\mathcal{T}\|\right) + e_j(t_k) \tag{8}$$

where $e_j = \tilde{I}_j(t_k) - E[\tilde{I}_j(t_k)]$, and $|\mathcal{A}_j|$ is the perimeter length of the type-j sensor's sensing area and is $2\pi r_j$ for a disk-shaped sensing area and $2r_j$ for a line-segment sensing area.

Consider the least square error estimators $\widehat{|\mathcal{T}|}$, $\widehat{\|\mathcal{T}\|}$, and $\hat{\alpha}$ for $|\mathcal{T}|$, $\|\mathcal{T}\|$, and α.

$$(\widehat{|\mathcal{T}|}, \widehat{\|\mathcal{T}\|}, \hat{\alpha}) = \arg\min_{|\mathcal{T}|,\|\mathcal{T}\|,\alpha} \sum_{k=1}^{m}\sum_{j} e_j(t_k)^2 \tag{9}$$

If $|\mathcal{A}_j|$ ($j = 1, 2, 3$) are different from each other, we can obtain explicit formulas of estimators that minimize the sum of square errors.

[Proposition of least square error estimators]

If $|\mathcal{A}_j|$ ($j = 1, 2, 3$) are different from each other, Eq. (9) has the following solution.

$$\widehat{|\mathcal{T}|} = \frac{2\pi}{C}\left\{\frac{\bar{I}_1(r_3^2 - r_2^2)}{\lambda_1} + \frac{\bar{I}_2(r_1^2 - r_3^2)}{\lambda_2} + \frac{\bar{I}_3(r_2^2 - r_1^2)}{\lambda_3}\right\} \tag{10}$$

$$\widehat{\|\mathcal{T}\|} = \frac{\bar{I}_1(r_2^2|\mathcal{A}_3| - r_3^2|\mathcal{A}_2|)}{\lambda_1 C} + \frac{\bar{I}_2(r_3^2|\mathcal{A}_1| - r_1^2|\mathcal{A}_3|)}{\lambda_2 C} + \frac{\bar{I}_3(r_1^2|\mathcal{A}_2| - r_2^2|\mathcal{A}_1|)}{\lambda_3 C} \tag{11}$$

$$\hat{\alpha} = \{\bar{I}_1(|\mathcal{A}_2| - |\mathcal{A}_3|)/\lambda_1 + \bar{I}_2(|\mathcal{A}_3| - |\mathcal{A}_1|)/\lambda_2 + \bar{I}_3(|\mathcal{A}_1| - |\mathcal{A}_2|)/\lambda_3\}/C, \tag{12}$$

where $C = r_1^2(|\mathcal{A}_2| - |\mathcal{A}_3|) + r_2^2(|\mathcal{A}_3| - |\mathcal{A}_1|) + r_3^2(|\mathcal{A}_1| - |\mathcal{A}_2|)$.

Proof: By replacing $e_j(t_k)$ with $\tilde{I}_j(t_k) - \lambda_j(\alpha r_j^2 + \frac{|\mathcal{A}_j|}{2\pi}|\mathcal{T}| + \|\mathcal{T}\|)$ in Eq. (9) and differentiating it with $|\mathcal{T}|$, $\|\mathcal{T}\|$, and $\hat{\alpha}$,

$$\begin{cases} \sum_{k,j}(\tilde{I}_j(t_k) - \lambda_j(\alpha r_j^2 + \frac{|\mathcal{A}_j|}{2\pi}|\mathcal{T}| + \|\mathcal{T}\|))(-\lambda_j\frac{|\mathcal{A}_j|}{2\pi}) = 0 \\ \sum_{k,j}(\tilde{I}_j(t_k) - \lambda_j(\alpha r_j^2 + \frac{|\mathcal{A}_j|}{2\pi}|\mathcal{T}| + \|\mathcal{T}\|))(-\lambda_j) = 0 \\ \sum_{k,j}(\tilde{I}_j(t_k) - \lambda_j(\alpha r_j^2 + \frac{|\mathcal{A}_j|}{2\pi}|\mathcal{T}| + \|\mathcal{T}\|))(-\lambda_j r_j^2) = 0. \end{cases} \tag{13}$$

That is,

$$\begin{cases} \sum_j(\bar{I}_j - \lambda_j(\alpha r_j^2 + \frac{|\mathcal{A}_j|}{2\pi}|\mathcal{T}| + \|\mathcal{T}\|))(-\lambda_j\frac{|\mathcal{A}_j|}{2\pi}) = 0 \\ \sum_j(\bar{I}_j - \lambda_j(\alpha r_j^2 + \frac{|\mathcal{A}_j|}{2\pi}|\mathcal{T}| + \|\mathcal{T}\|))(-\lambda_j) = 0 \\ \sum_j(\bar{I}_j - \lambda_j(\alpha r_j^2 + \frac{|\mathcal{A}_j|}{2\pi}|\mathcal{T}| + \|\mathcal{T}\|))(-\lambda_j r_j^2) = 0. \end{cases} \tag{14}$$

Thus, if Eq. (15) with $j = 1, 2, 3$ has a set of solutions ($\widehat{|\mathcal{T}|}$, $\widehat{\|\mathcal{T}\|}$, $\hat{\alpha}$), the above three equations are satisfied and $\widehat{|\mathcal{T}|}$, $\widehat{\|\mathcal{T}\|}$, and $\hat{\alpha}$ become the least square error estimator.

$$\bar{I}_j = \lambda_j\left(\hat{\alpha} r_j^2 + \frac{|\mathcal{A}_j|}{2\pi}\widehat{|\mathcal{T}|} + \widehat{\|\mathcal{T}\|}\right) \tag{15}$$

Equations (10), (11), and (12) satisfy Eq. (15) with $j = 1, 2, 3$. □

Equations (10) and (11) are unbiased estimators. If we assume that Eq. (7) is valid, we can obtain a similar estimation method by using four types of sensors that have different $|\mathcal{A}_j|$ $(1 \le j \le 4)$ from each other.

Therefore, we obtain the following estimation method. (1) At t_k, receive the report $I_i(t_k)$ from each sensor whose location is unknown. (2) Calculate the sum $\tilde{I}_j(t_k) = \sum_{i=n_{j-1}+1}^{n_j} I_i(t_k)$ for each sensor type $(j = 1, 2, 3)$. (3) At t_m, take the time average from t_1 to t_m to obtain $\bar{I}_j = \sum_{k=1}^{m} \tilde{I}_j(t_k)/m$ $(j = 1, 2, 3)$. (4) Calculate Eqs. (10), (11), and (12) to obtain the estimators for $|\mathcal{T}|$, $\|\mathcal{T}\|$, and α.

Remark:

We should note that the estimators are not dependent on the movement model of the target object. If a target object moves slowly, the sensor reports may have a large correlation with the previous reports. Therefore, to make the estimates accurate, more data may be needed when the target object moves slowly. However, the estimation method does not depend on the speed or movement of the target object. In addition, in general, if the total number of sensors is fixed, high-density sensor deployment in a small area is equivalent to low-density deployment in a large area. If the current position of the target object does not overlap with that in the previous measurement epoch, the current sensory reports become independent of the previous reports. Then, the estimation variance is determined only by the total number of reports. Because the total number of reports is fixed if the total number of sensors and the number of measurement epochs are fixed, high-density sensor deployment in a small area is equivalent to low-density deployment in a large area. Numerical examples for various speed and those for various sensor densities are shown in [15].

5. Numerical Examples

This section illustrates the results of computer simulations executed to check the validity of our developed estimation method. The following conditions were set for the simulations. (1) Each simulation run length was 100 units of time. (2) Each sensor senses and sends a report at every unit of time, i.e., $t_k = 1, 2, \cdots, 100$. (3) One thousand simulation runs were performed to obtain each point in each graph. (4) $\lambda_i = 1$ for all i if it is not explicitly specified. (5) The target object moved 1 unit length per unit time in a 200×200 square unit-length area if not explicitly specified. (6) Sensors were deployed in a homogeneous spatial Poisson process.

5.1 Estimations for T-Shaped and Cap-Shaped Target Objects

This subsection shows the estimation results for a target object that is T-shaped or cap-shaped (Fig. 3), where the sensing area is line-segment-shaped. In the numerical examples, we used the sets of parameters listed in Table 1 for the target objects.

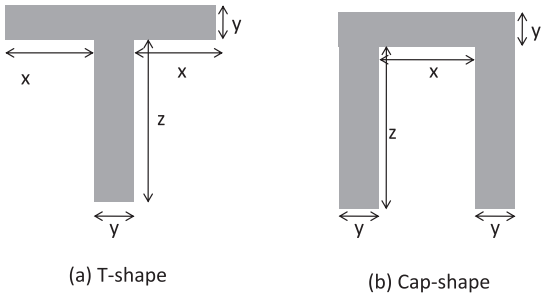

Fig. 3 Examples of target objects.

Table 1 Parameter values of target object.

	T-shaped			Cap-shaped		
No.	x	y	z	x	y	z
1	0	0.5	10	0	0.5	10
2	0.5	0.5	10	0.5	0.5	10
3	3	0.5	10	3	0.5	10
4	10	0.5	10	10	0.5	10
5	0	3	10	0	3	10
6	0.5	3	10	0.5	3	10
7	3	3	10	3	3	10
8	10	3	10	10	3	10
9	0	10	10	0	10	10
10	0.5	10	10	0.5	10	10
11	3	10	10	3	10	10
12	10	10	10	10	10	10

The estimation method described in the previous section was used. That is, the perimeter length, size, and parameter α of the target object were estimated through Eqs. (10), (11), and (12).

The estimated results for T-shaped target objects with error size bars are shown in Figs. 4 and 6, and those for cap-shaped target objects are in Figs. 5 and 7. The error sizes used here are the standard deviations of the estimates under the assumption of mutual independence among $\bar{I}_1$, $\bar{I}_2$, and $\bar{I}_3$ from each other while the observed variations of the sample $\bar{I}_i$ are used (see the Appendix for details). Error sizes were very small for these examples and are sometimes not visible in these figures.

The estimation of $\|\mathcal{T}\|$ and $|\mathcal{T}|$ was accurate through our method for T-shaped target objects even when they were not r-tractable for some r. This suggests that we can relax the conditions making Eq. (2) valid. The accuracy remains good for the combination of (r_1, r_2, r_3).

The estimation of $\|\mathcal{T}\|$ and $|\mathcal{T}|$ is also accurate through the proposed method for cap-shaped target objects, except for a few cases. The most difficult case is the estimation for a target object with $x = 0.5$ (No. = 2, 6, 10). For this case, there is no combination of line-segment-shaped sensing areas where the target object is r-tractable for $r = r_1, r_2, r_3$.

An interesting feature is found in the estimation of α. α is determined only by the interior angles of the target objects. For T-shaped target objects with $x > 0$, $\alpha = -1/2\pi$ for a line-segment sensing area. For T-shaped target objects with $x = 0$ (i.e., when T-shaped target objects become rect-

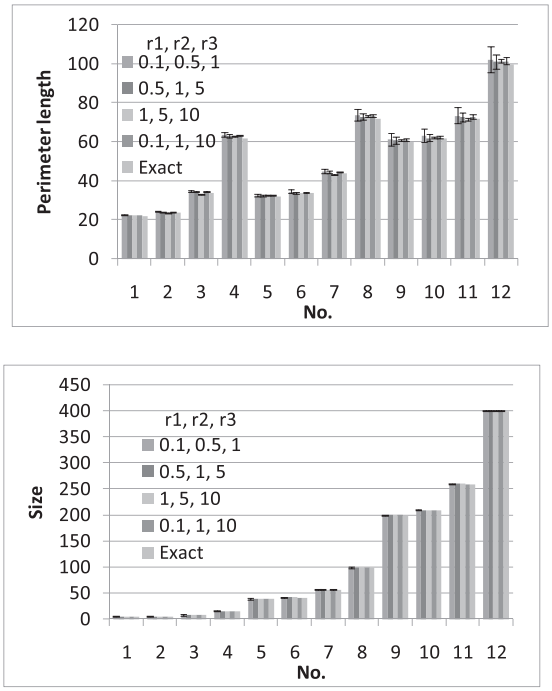

Fig. 4 Estimated size $\|\mathcal{T}\|$ and perimeter length $|\mathcal{T}|$ of T-shaped target object by line-segment-shaped sensing areas.

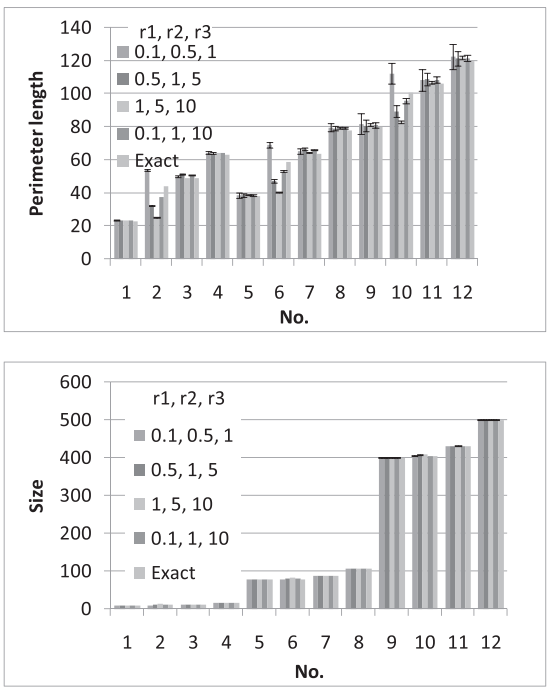

Fig. 5 Estimated size $\|\mathcal{T}\|$ and perimeter length $|\mathcal{T}|$ of cap-shaped target object by line-segment-shaped sensing areas.

angular), $\alpha = 0$ for a line-segment sensing area. Thus, there is a jump of α at $x = 0$. However, the sensor cannot detect the jump at $x = 0$. When x is only slightly greater than 0 (small $x > 0$), the estimated α can approximately be equal to α at $x = 0$ or it takes an incorrect value. That is, the sensor

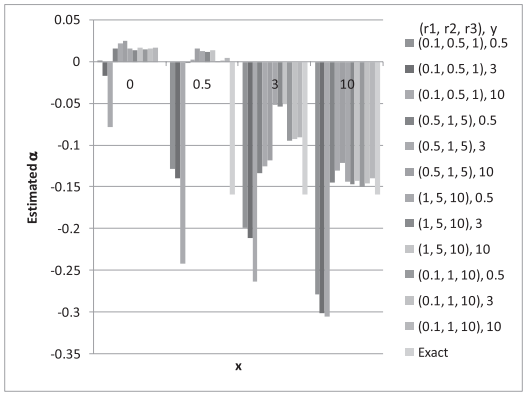

Fig. 6 Estimation of α for T-shaped target object by line-segment-shaped sensing areas.

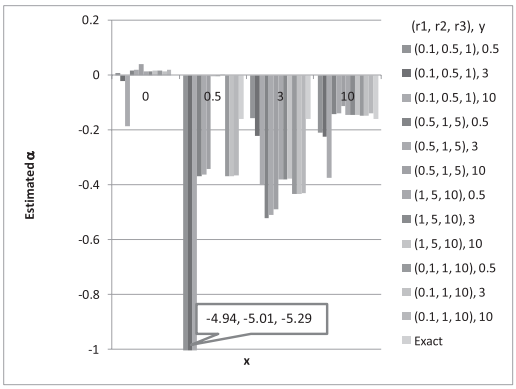

Fig. 7 Estimation of α for cap-shaped target object by line-segment-shaped sensing areas.

cannot distinguish between a T-shape (cap-shape) of small $x > 0$ and a rectangle or it becomes disorientated.

For the small sensing area combination $(r_1, r_2, r_3) = (0.1, 0.5, 1)$, even for small $x > 0$, $\hat{\alpha}$ at $x > 0$ is different from that at $x = 0$. Thus, this small sensing area combination can sensitively detect the shape for small $x > 0$. However, this combination is likely to yield estimates of α that are too small. This is a side effect of the sensitive detection of the T-shape. When $x > 0$ is not small, other combinations are better for estimating α.

Similarly, for the disk-shaped sensing area, the estimated results for T-shaped target objects with error size bars are shown in Figs. 8 and 10, and those for cap-shaped target objects are in Figs. 9 and 11. The results using the disk-shaped sensing area are quite similar to those using the line-segment-shaped sensing area, although the error sizes of the former are a little smaller than that of the latter.

5.2 Target Object with Holes

This subsection checks the validity of corollaries through a numerical example.

Consider a doughnut-shaped target object with the outer radius r_o and the inner radius a. This target object

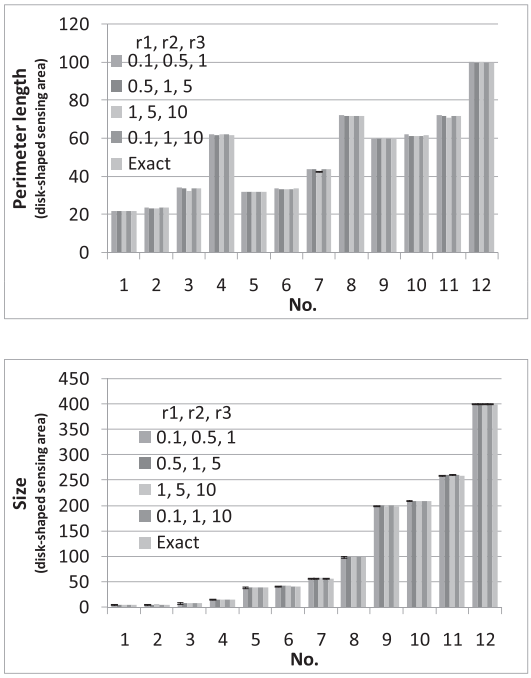

Fig. 8 T-shaped target object estimation by disk-shaped sensing areas.

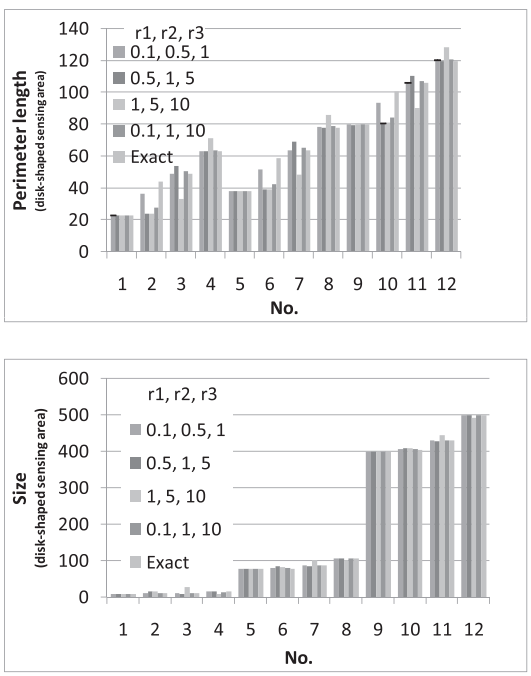

Fig. 9 Cap-shaped target object estimation by disk-shaped sensing areas.

can be considered to be formed from an original disk-shaped target object of radius r_o with an added hole of radius a. Because the original target object is convex, Eq. (1) holds. In addition, by applying Eq. (3), we can obtain the theoretical value T_v of $\|\mathcal{D}\|$. We compare the theoretical values T_v and the simulation sample $\tilde{I}_i/\lambda_i$, which is the expected value of $\|\mathcal{D}\|$. If Eq. (3) holds true, these two values will show good agreement.

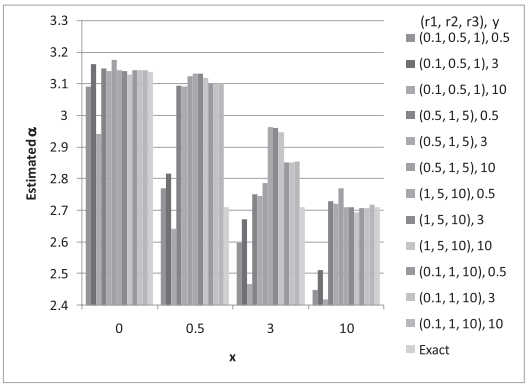

Fig. 10 Estimation of α for T-shaped target object by disk-shaped sensing areas.

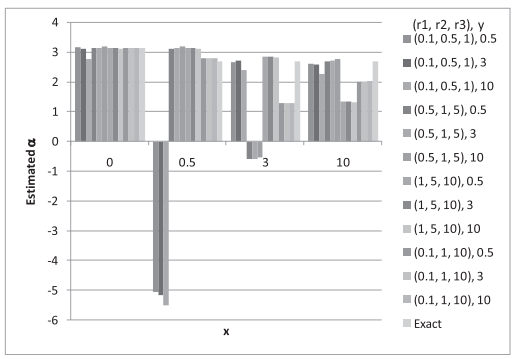

Fig. 11 Estimation of α for cap-shaped target object by disk-shaped sensing areas.

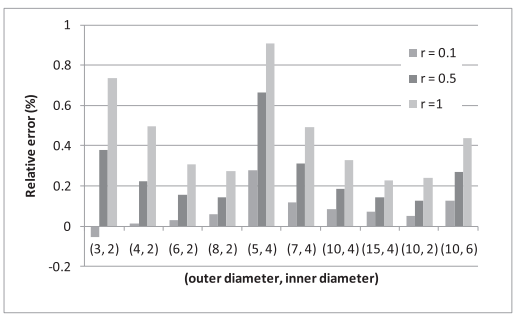

Fig. 12 Relative errors for doughnut-shaped target object (line-segment-shaped sensing area).

The relative errors $100(\tilde{I}_i/\lambda_i/T_v - 1)$ in percentages are plotted in Fig. 12. The relative error size is small and is less than 1% for all cases. Thus, we can conclude that the [Corollary for target object containing disk-shaped holes with line-segment-shaped sensing areas] is valid. Actually, there is a small positive bias. This seems to be because the simulation uses a circular-sector-shaped sensing area with a very small central angle instead of the line segment.

For a fixed inner radius, as the outer radius (outer diameter) increases, the relative error decreases. In contrast, for a fixed outer radius, as the inner radius (inner diameter) increases, the relative error also increases. In addi-

tion, a smaller r, i.e., a smaller sensing area (a shorter line-segment-shaped sensing area) provides more accurate results.

Then, we check the validity of the [Corollary for target object containing holes with line-segment-shaped (disk-shaped) sensing areas]. The target object is a disk of radius b with a square hole at the center of the disk, where the length of a side of the square is a. Disk-shaped sensing areas or line-segment-shaped sensing areas are assumed. We obtain a theoretical value T_v of $\|\mathcal{D}\|$ by applying Eq. (2) with $\alpha = -1/\pi$ for a line-segment-shaped sensing area and Eq. (6) with $\alpha = \pi - 4$ for a disk-shaped sensing area. Considering that the sampled value of $\|\mathcal{D}\|$ is $\tilde{I}_j/\lambda$, we plot the relative errors $100(\tilde{I}_i/\lambda_i/T_v - 1)$ in percentages in Fig. 13. We find that the relative error is small and is less than 1.3% for all cases satisfying the condition of $2r$-tractable (r-tractable). The figure shows that a smaller sensing area and a large target object yields more accurate results. As a reference, the relative errors for the cases not satisfying the condition of $2r$-tractable (r-tractable) are shown in Fig. 14. There, the relative error is much larger than in the cases satisfying the condition of $2r$-tractable (r-tractable); it is larger by more than 10%, sometimes reaching more than hundreds of percents. In particular, disk-shaped sensing areas show results that are not as good as those obtained by line-segment-shaped sensing areas.

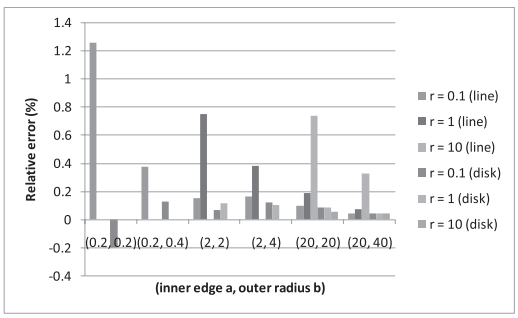

Fig. 13 Relative errors for disk-shaped target object with square hole (condition satisfied).

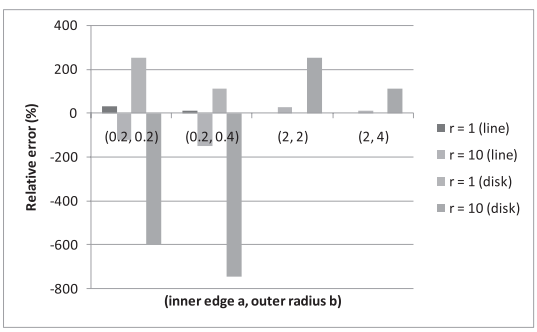

Fig. 14 Relative errors for disk-shaped target object with square hole (condition not satisfied).

5.3 Sensing Area of General Shape

Finally, we check the validity of Eq. (7) through a numerical example. The target object in this numerical example is assumed to be T-shaped or cap-shaped. For this target object shape, we find that $\beta_2 = 1/2$. When a T-shape or cap-shape becomes rectangular (that is, when $x = 0$), $\beta_2 = 0$.

Thus, we plot $(\|\mathcal{D}\| - \|\mathcal{T}\| - |\mathcal{A}| \cdot |\mathcal{T}|/2\pi - \beta_2\|\mathcal{A}\|)$ as a function of $|\mathcal{A}|^2$ by replacing $\|\mathcal{D}\|$ with $\tilde{I}_i/\lambda_i$ and using exact values of $\|\mathcal{T}\|$ and $|\mathcal{T}|$. If the plots are in a straight line, we can construe that β_1 is constant and that Eq. (7) is valid for various sensing areas. The sensing area used for this example has circular-sector-shapes with the radius r and the central angle η.

Figure 15 plots the results for T-shaped target objects, and Fig. 16 plots the results for cap-shaped target objects estimated by sector-shaped sensing areas with the radius $r = 0.1, 0.5, 1, 5, 10$ and the central angle $\eta = \pi/2, \pi$. We can see that the plotted points are almost on four lines. Thus, Eq. (7) seems to be valid. However, there should only be two lines if the parameter β_1 is determined only by interior angles. Each line corresponds to each value of x in these figures. The line corresponding to $x = 0$ (the rectangular target object) is far from the other three lines corresponding to $x > 0$ (T-shaped

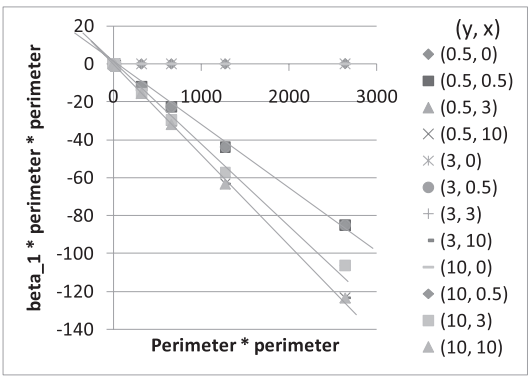

Fig. 15 T-shaped target object estimation by general sensing-area shapes.

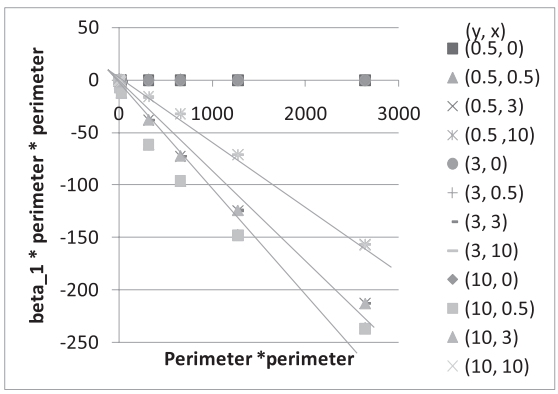

Fig. 16 Cap-shaped target object estimation by general sensing-area shapes.

or cap-shaped target objects). This suggests that, although β_1 is mainly determined by interior angles, it also depends on other shape-dependent factors. This may be an indication for a new estimation method dependent on shape.

6. Conclusion

We presented a method for estimating the parameters of a target object that may be non-convex. These parameters are size, perimeter length, and parameter(s) determined only by interior angles. This method uses the reports sent by networked sensors whose locations are unknown. Each report from each sensor is binary information on whether or not the sensor detects the target object in its sensing area, which is disk-shaped or line-segment-shaped. It is counterintuitive that the binary information from the sensors at unknown locations can estimate the parameters related to its shape, but our method produced accurate estimation results in the numerical examples. In addition, we proposed a unified equation applicable to generic sensing areas, including disk-shaped and line-segment-shaped sensing areas and non-convex target objects. A numerical example showed that the unified equation may hold true for a general sensing-area shape and non-convex target objects.

We implicitly assumed that there is a single target object in the monitored region. In future studies, we will present results for possible multiple target objects in a monitored region [16].

References

[1] G.J. Pottie and W.J. Kaiser, "Wireless integrated network sensors," Commun. ACM, vol.43, no.5, pp.51–58, May 2000.
[2] I.F. Akyildiz, W. Su, Y. Sankarasubramaniam, and E. Cayirci, "A survey on sensor networks," IEEE Commun. Mag., vol.40, no.8, pp.102–114, 2002.
[3] B.W. Cook, S. Lanzisera, and K.S.J. Pister, "SoC issues for RF smart dust," Proc. IEEE, vol.94, no.6, pp.1177–1196, June 2006.
[4] H. Saito, M. Umehira, O. Kagami, and Y. Kado, "Wide area ubiquitous network: Network operator's view of sensor network," IEEE Commun. Mag., vol.46, no.12, pp.112–120, 2008.
[5] H. Saito, S. Shioda, and J. Harada, "Shape and size estimation using stochastically deployed networked sensors," IEEE SMC 2008, Singapore, 2008.
[6] P. Hall, Introduction to the Theory of Coverage Processes, John Wiley & Sons, 1988.
[7] L. Lazos and R. Poovendran, "Stochastic coverage in heterogeneous sensor networks," ACM Sensor Networks, vol.2, no.3, pp.325–358, 2006.
[8] B. Liu and D. Towsley, "A study on the coverage of large-scale sensor networks," IEEE Mobile Ad-hoc and Sensor Systems, 2004.
[9] P. Manohar, S.S. Ram, and D. Manjunath, "On the path coverage by a non-homogeneous sensor field," IEEE Globecom, 2006.
[10] H. Saito, K. Shimogawa, S. Shioda, and J. Harada, "Shape estimation using networked binary sensors," INFOCOM, 2009.
[11] H. Saito, Y. Arakawa, K. Tano, and S. Shioda, "Experiments on binary sensor networks for estimation of target perimeter and size," IEEE SECON 2009 Workshop, Rome, 2009.
[12] D. Tian and N. Georganas, "A coverage-preserving node scheduling scheme for large wireless sensor networks," First ACM Workshop on Wireless Sensor Networks and Applications, pp.32–41, 2002.
[13] F. Ye, G. Zhong, S. Lu, and L. Zhang, "Peas: A robust energy conserving protocol for long-lived sensor networks," IEEE ICDCS, 2003.
[14] S. Shakkottai, R. Srikant, and N. Shroff, "Unreliable sensor grids: Coverage, connectivity and diameter," Proc. IEEE INFOCOM, 2003.
[15] H. Saito, S. Tanaka, and S. Shioda, "Estimating parameters for non-convex target object using networked binary sensors," IEEE SUTC, 2010.
[16] H. Saito, S. Shimogawa, S. Tanaka, and S. Shioda, "Estimating parameters of multiple heterogeneous target objects using composite sensor nodes," IEEE Trans. Mobile Computing, to be published.

Appendix A: Proof of Proposition for Line-Segment-Shaped Sensing Areas [15]

A.1 Definitions

We introduce some definitions for the proof of the proposition. We assume that the target object boundary is a simple closed curve consisting of line segments.

Definition 1.

Each line segment of the exterior boundary of the target object is called a boundary line segment.

Definition 2.

Consider a boundary line segment L. The r-relevant area of the boundary line segment L is the area attached to the boundary line segment L outside the target object and consists of three parts (Fig. A· 1). The first part is the rectangle. One side of the rectangle is the boundary line segment L. The length of the sides vertical to the boundary line segment L is r. The other two parts are circular-sector-shaped areas. Their centers are located at the two end points of the boundary line segment L, the arch radius is r, and the center angle is $\pi/2$. They are attached to the outside of the rectangle.

We use the symbols $\circ$ and $\bullet$ to denote whether or not two boundary line segments are adjacent. That is, for two boundary line segments L and L', $L \circ L'$ means they are adjacent ($L \cap L' \neq \emptyset$) and $L \bullet L'$ means they are not adjacent ($L \cap L' = \emptyset$).

Definition 3.

Consider the r-relevant area of a boundary line segment L. If the r-relevant area does not include any point of any boundary line segment L' where $L' \bullet L$, the r-relevant area

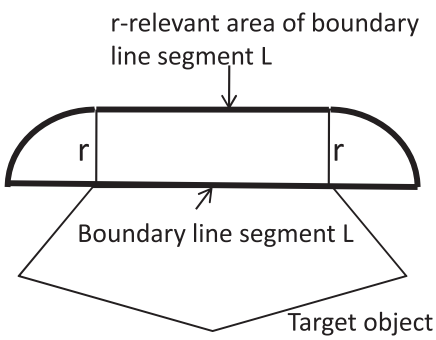

Fig. A· 1 Relevant area of boundary line segment.

is called r-tractable. The target object is called r-tractable if all r-relevant areas of all the boundary line segments of the target object are tractable.

For any r, a convex target object is r-tractable. A non-convex target object, however, may or may not be r-tractable. For example, the T-shaped or cap-shaped target objects shown in Fig. 3 are r-tractable if $x, y, z > r$. They are not r-tractable if $\min(x, y, z) \leq r$.

Definition 4.

Consider a boundary line segment. The detectable parallelogram generated from the boundary line segment L with the interior angle ξ is the parallelogram attached to the boundary line segment L outside the target object (Fig. A· 2). One of the sides of the parallelogram is the boundary line segment L. The length of the sides that are not parallel to the boundary line segment is r. The interior angle between the boundary line segment L and the right side of the parallelogram when the side attached to the boundary line segment L is located at the bottom is ξ, where $0 < \xi < \pi$. The orientation of the boundary line segment is the counterclockwise trace of the boundary. When we consider a boundary line segment and are conscious of its orientation, we call it an oriented boundary line segment.

For a fixed rotation angle θ of the sensing area, the detectable area is the sum of the target object and all the detectable parallelograms generated from some of the boundary line segments (Fig. A· 3). Note that the boundary line segments for which angles ψ are between θ and $\theta + \pi$ do not generate the detectable parallelogram. Here, the angle ψ of the boundary line segment L is defined by the angle between the x-axis and the oriented boundary line segment L. As a result, the interior angle ξ of the detectable parallelogram is $\xi = \psi - \theta - \pi \pmod{2\pi}$.

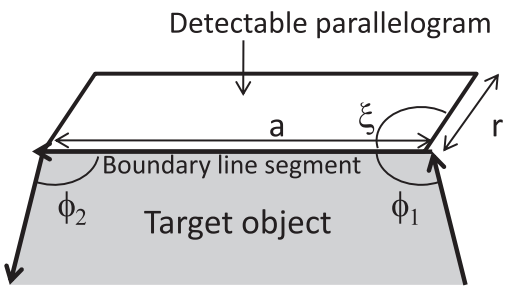

Fig. A· 2 Detectable parallelogram.

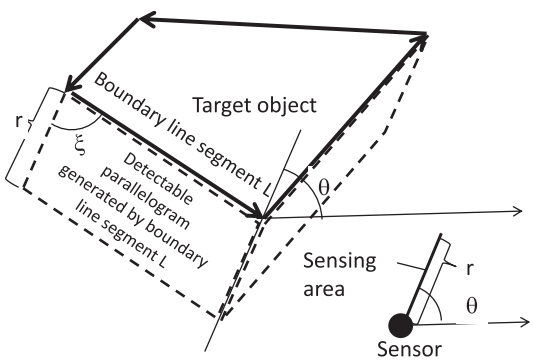

Fig. A· 3 Detectable area with line-segment-shaped sensing area.

A.2 Proof

Consider an oriented boundary line segment L. Let ϕ_1 be the interior angle at its root end point and ϕ_2 be that of its top end point. Assume that the boundary line segment generates a detectable parallelogram with the interior angle ξ (Fig. A· 2). Consider another boundary line segment L' (Fig. A· 4). If there are overlaps between the detectable parallelogram generated by the boundary line segment L and that generated by another boundary line segment L', a part of the boundary line segment L' must be in the detectable parallelogram of the boundary line segment L.

Note that the detectable parallelogram is included in the r-relevant area. Because the target object is r-tractable, there can be no point on any boundary line segment L'' in the detectable parallelogram generated by the boundary line segment L, where $L'' \bullet L$. Therefore, the boundary line segment L' must be adjacent to the boundary line segment L, i.e., $L' \circ L$. If any boundary line segment L' that satisfies $L' \circ L$ intersects the detectable parallelogram generated from the boundary line segment L, these two boundary segments cause an overlap. The overlap is between the detectable parallelogram and the target object itself (Fig. A· 5).

When $\phi_1 + \xi > 2\pi$ for $0 < \phi_1 < 2\pi$ and $0 < \xi < \pi$, the detectable parallelogram has an overlap where ξ is the interior angle of the detectable parallelogram. Thus, $\phi_1 > \pi$. As shown in Fig. A· 5, the size of the overlap is given by

$$\begin{cases} r\cos(\pi/2-\xi)(-r\sin(\pi/2-\xi) \\ \quad +r\cos(\pi/2-\xi)\tan(\phi_1-3\pi/2))/2, & \text{for } 0<\xi<\pi/2, \\ r\sin(\pi-\xi)(r\cos(\pi-\xi) \\ \quad +r\sin(\pi-\xi)\tan(\phi_1-3\pi/2))/2, & \text{for } \pi/2\leq\xi<\pi, \end{cases}$$

$= -r^2 \sin\xi \sin(\xi + \phi_1)/(2\sin\phi_1)$.

Similarly, when $\phi_2 + (\pi - \xi) > 2\pi$, the detectable parallelogram has another overlap. Then, $\phi_2 > \pi$. The size of this overlap is $-r^2 \sin\xi \sin(\pi - \xi + \phi_2)/(2\sin\phi_2)$.

When $\phi_1 + \xi > 2\pi$ and $\phi_2 + \pi - \xi > 2\pi$, there are two overlaps that do not overlap each other because the target object is r-tractable.

By removal of the size of the overlapped areas, the ac-

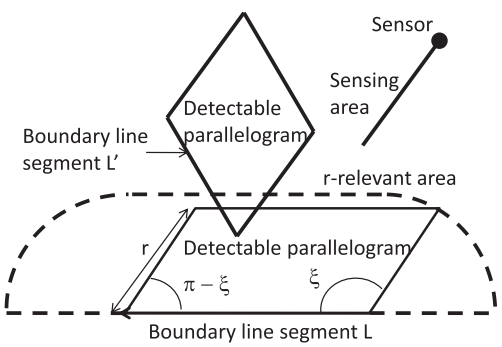

Fig. A· 4 Detectable parallelogram and r-relevant area.

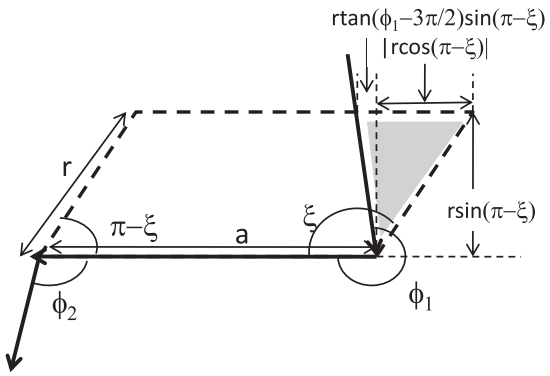

$$\phi_1 + \xi > 2\pi,\ \phi_2 + \pi - \xi < 2\pi$$

Fig. A· 5 Overlap of detectable area with line-segment-shaped sensing area.

tual size $s(a, \phi_1, \phi_2, \xi)$ of this detectable parallelogram generated by this boundary line segment is given by $ar \sin\xi + r^2 \sin\xi\{\mathbf{1}(\phi_1 + \xi > 2\pi)\sin(\xi + \phi_1)/\sin\phi_1 + \mathbf{1}(\phi_2 + \pi - \xi > 2\pi)\sin(\pi - \xi + \phi_2)/\sin\phi_2\}/2$, where the length of this boundary line segment is a. Then,

$$\begin{aligned}&\int_0^\pi s(a, \phi_1, \phi_2, \xi)d\xi \\ &= 2ar + \frac{r^2}{4}\{\mathbf{1}(\pi < \phi_1)(-1 + (-\pi + \phi_1)\cos\phi_1/\sin\phi_1) \\ &\quad + \mathbf{1}(\pi < \phi_2)(-1 + (-\pi + \phi_2)\cos\phi_2/\sin\phi_2)\}. \quad (\text{A}\cdot 1)\end{aligned}$$

Let a_i be the length of the i-th boundary line segment, $\phi_{i,1}$ and $\phi_{i,2}$ be the interior angles at the root and top of the i-th boundary line segment, respectively, and ξ_i be the interior angle of the detectable parallelogram generated from the i-th boundary line segment. Then,

$$\begin{aligned}\|\mathcal{D}\| &= \|\mathcal{T}\| + \frac{1}{2\pi}\sum_i \int_0^{2\pi} s(a_i, \phi_{i,1}, \phi_{i,2}, \xi_i)d\theta \\ &= \|\mathcal{T}\| + \frac{1}{2\pi}\sum_i \int_0^{\pi} s(a_i, \phi_{i,1}, \phi_{i,2}, \xi_i)d\xi_i \\ &= \|\mathcal{T}\| + \frac{1}{2\pi}\sum_i \left(2a_i r + \frac{r^2}{4}(\alpha_{i,1} + \alpha_{i,2})\right) \\ &= \|\mathcal{T}\| + r|\mathcal{T}|/\pi + \alpha r^2, \quad (\text{A}\cdot 2)\end{aligned}$$

where $\alpha_{i,j} = \mathbf{1}(\pi < \phi_{i,j})(-1 + (-\pi + \phi_{i,j})\cos\phi_{i,j}/\sin\phi_{i,j})$ $(j = 1, 2)$, $\alpha = \frac{1}{4\pi}\sum_i \mathbf{1}(\pi < \phi_i)\{-1 + (-\pi + \phi_i)\cos\phi_i/\sin\phi_i\}$. □

Appendix B: Proof of Proposition for Disk-Shaped Sensing Areas

B.1 Definitions

In additions to the definitions in Appendix A, we introduce some definitions for the proof of the proposition for disk-shaped sensing areas. We assume that the target object boundary is a simple closed curve consisting of line segments.

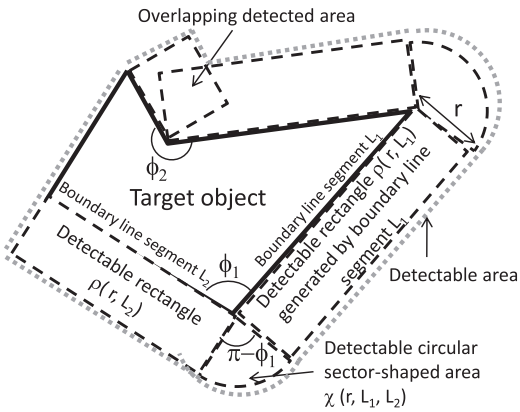

Fig. A· 6 Detectable rectangles and circular-sector-shaped areas.

Definition 5.

Consider a boundary line segment L (Fig. A· 6). The r-detectable rectangle $\rho(r, L)$ generated from the boundary line segment L is the rectangular area attached to the boundary line segment outside of the target object. One of the sides of the rectangle is the boundary line segment. The length of the sides vertical to the boundary line segment is r.

Definition 6.

For a convex vertex, we define an r-detectable circular-sector-shaped area $\chi(r, L, L')$. Its center is located at the vertex, which is the common end point of boundary line segments L and L' where $L \circ L'$, the arch radius is r, and the center angle is $\pi - \phi$, where ϕ is the interior angle of the vertex. The circular-sector-shaped area is attached to and lies between two detectable rectangles $\rho(r, L)$ and $\rho(r, L')$ (Fig. A· 6).

B.2 Preliminaries for Proof of Proposition for Disk-Shaped Sensing Areas

To prove Proposition for disk-shaped sensing areas, we provide the following lemmas.

Lemma 1.

Assume that the sensing area of each sensor is a disk of radius r. The target object $\mathcal{T}$ is $2r$-tractable, and its boundary is a simple closed curve consisting of line segments. Consider a boundary line segment L of the target object and its generated r-detectable rectangle $\rho(r, L)$. $\rho(r, L)$ does not overlap with any other r-detectable rectangles $\rho(r, L')$ that satisfy $L' \bullet L$ or any detectable circular sector-shaped area $\chi(r, L_1, L_2)$ that $L_1, L_2 \neq L$. The overlap of $\rho(r, L)$ and $\chi(r, L_1, L_2)$ that L_1 or $L_2 = L$ is the common line segment length r and its size is 0.

Proof of Lemma 1. Around the detectable rectangle, define the possible overlap area: $\{(x, y) | \min_{(a,b)}(x-a)^2 + (y-b)^2 \leq r^2, (a, b) \in \rho(r, L)\}$. As shown in Fig. A· 7, we can plot the possible overlap area by drawing circles of radius r around the detectable rectangle.

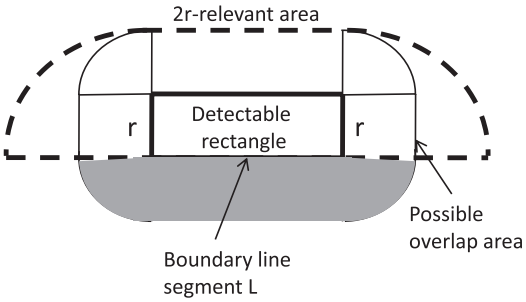

Fig. A· 7 Possible overlap area.

If no point of a boundary line segment $L'(\neq L)$ is in the possible overlap area, a detectable rectangle $\rho(r, L')$ or a detectable circular sector-shaped area $\chi(r, L', L'')$ $(L'' \neq L)$ cannot overlap with $\rho(r, L)$. Conversely, if there is a point of a boundary line segment L' in the possible overlap area, a detectable rectangle $\rho(r, L')$ or a detectable circular sector-shaped area $\chi(r, L', L'')$ may overlap with the detectable rectangle $\rho(r, L)$ generated from the boundary line segment L. Thus, we focus on a boundary line segment that has a point in the possible overlap area.

In the remainder of this proof, we take the following steps. The first step considers the shaded area (i.e., the area in the possible overlap area outside of the $2r$-relevant area) in Fig. A· 7. The second step considers the intersection area of the possible overlap area and the $2r$-relevant area. In each of these steps, we will show that $\rho(r, L)$ does not overlap with $\rho(r, L')$ where $L' \bullet L$ and that $\rho(r, L)$ does not overlap with $\chi(r, L_1, L_2)$ where $L_1, L_2 \neq L$. We should note that the possible overlap area is covered by the two areas that are considered in these two steps. As the final step, we will show that there is no overlap between a detectable rectangle $\rho(r, L)$ and a detectable circular sector-shaped area $\chi(r, L_1, L_2)$ where L_1 or $L_2 = L$.

As the first step, consider the shaded part of the possible overlap area in Fig. A· 7. The shaded area is outside of the $2r$-relevant area of the boundary line segment L. Assume there is a point of a boundary line segment L' in the shaded area where $L' \bullet L$. If $\rho(r, L')$ and $\rho(r, L)$ overlap each other, the $2r$-relevant area of the boundary line segment L' includes a part of the boundary line segment L. This is a contradiction of the definition of the $2r$-relevant area. Thus, $\rho(r, L')$ does not overlap with $\rho(r, L)$.

Assume that there is a convex vertex shared by two boundary line segments L_1 and L_2 in the shaded area and that the vertex is the center of a detectable circular sector-shaped area $\chi(r, L_1, L_2)$ $(L_1, L_2 \neq L)$. First, we consider the case that $L_1 \circ L$. We can easily show that a circular sector-shaped area $\chi(r, L_1, L_2)$ whose center is in the shaded area and of which one line segment L_1 is adjacent to L cannot overlap with $\rho(r, L)$ without overlapping of $\rho(r, L)$ and $\rho(r, L_2)$. Note that $L_2 \bullet L$. Due to the first step mentioned above, $\rho(r, L)$ and $\rho(r, L_2)$ cannot overlap each other. Thus, the circular sector-shaped area $\chi(r, L_1, L_2)$ described just above cannot overlap with $\rho(r, L)$

Next, we consider the case that $L_1, L_2 \bullet L$. If $\chi(r, L_1, L_2)$ overlaps with $\rho(r, L)$, at least one of two $2r$-relevant areas of two boundary line segments L_1 and L_2 includes a part of the boundary line segment L. This is again a contradiction of the definition of the $2r$-relevant area. Thus, a detectable circular sector-shaped area whose center is in the shaded area does not overlap with $\rho(r, L)$. As a result, a boundary line segment that has a point in the shaded area (the part of the possible overlap area that is outside of the $2r$-relevant area of the boundary line segment L) cannot make areas that overlap with the detectable rectangle $\rho(r, L)$.

As the second step, consider the remaining part of the possible overlap area (i.e., the non-shaded area included in the possible overlap area). This part is covered by the $2r$-relevent area. Thus, there is no point on a boundary line segment L' where $L' \bullet L$. Therefore, the detectable rectangle $\rho(r, L)$ has no overlap with detectable rectangles $\rho(r, L')$ or circular sector-shaped areas $\chi(r, L_1, L_2)$ where $L' \bullet L$ and $L_1, L_2 \neq L$.

Finally, we should note that there is no overlap between $\rho(r, L)$ and $\chi(r, L_1, L_2)$ except for two common line segments in their boundaries where L_1 or $L_2 = L$ because of the definition of the detectable circular sector-shaped area.

Consequently, the r-detectable rectangle $\rho(r, L)$ does not overlap with other r-detectable rectangles $\rho(r, L')$ $(L \bullet L')$ or any detectable circular sector-shaped area $\chi(r, L_1, L_2)$. □

Lemma 2. Assume that the sensing area of each sensor is a disk of radius r. The target object $\mathcal{T}$ is $2r$-tractable, and its boundary is a simple closed curve consisting of line segments. Consider detectable circular sector-shaped areas. There are no intersections between two such areas.

Proof of Lemma 2. Consider a detectable circular sector-shaped area with the arch radius r at a vertex V for which the interior angle is ϕ and for which boundary line segments are L_1 and L_2. (Note $0 < \phi < \pi$.)

Lemma 1 has already concluded that an overlap cannot occur between a detectable rectangle and a detectable circular sector-shaped area. This implies that any straight line segment part of a detectable circular sector-shaped area does not have intersections with other detectable circular sector-shaped areas. Thus, we can focus on analyzing whether there are intersections between the circular part of the detectable circular sector-shaped area and that of another detectable circular sector-shaped area without any intersection of their straight-line-segments parts.

Consider the relationship between the detectable circular sector-shaped area and the $2r$-relevant area. If $\pi/2 \leq \phi < \pi$, the detectable circular sector-shaped area is included in the $2r$-relevent areas of the boundary line segments L_1 and L_2 (Fig. A· 8). If $\phi < \pi/2$, any point in the detectable circular sector-shaped area is included in at least one of the $2r$-relevent areas of the boundary line segments L_1 and L_2. That is, the detectable circular sector-shaped area for which circular radius is r and for which the center is the vertex V is included in a circular sector-shaped area Υ, whose circular radius is $2r$ and center is vertex V. Υ is the union of two circular sector-shaped areas of the $2r$-relevent areas of the

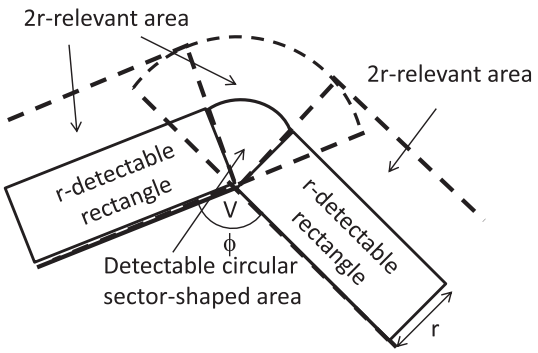

Fig. A· 8 Detectable circular sector-shaped area and relevant areas.

boundary line segments L_1 and L_2. Thus, there are no intersections between the circular part of the detectable circular sector-shaped area and that of another detectable circular sector-shaped area without any of the straight-line-segment parts intersecting. □

Lemma 3.

Assume that the sensing area of each sensor is a disk of radius r. The target object $\mathcal{T}$ is $2r$-tractable, and its boundary is a simple closed curve consisting of line segments. Consider two adjacent detectable rectangles $\rho(r, L)$ and $\rho(r, L')$ generated from boundary line segments L and L' where $L \circ L'$. Let ϕ be the interior angles between L and L'. The size of the overlapped area made by these two adjacent detectable rectangles is $-\mathbf{1}(\phi > \pi)r^2(1 + \cos\phi)/\sin\phi$.

Proof of Lemma 3. Overlaps between two adjacent detectable rectangles occur only when $\pi < \phi (< 2\pi)$. We need to consider two cases: (i) $\pi < \phi \leq 3\pi/2$ and (ii) $3\pi/2 \leq \phi < 2\pi$ (Fig. A· 9). Because the lengths of the boundary line segments are larger than $-r(\cos\phi + 1)/\sin\phi$, the overlap area shape is as shown in Fig. A· 9. Here, the lengths of the two sides of the right-angled triangle, which is half of the overlap area, are r and $-r(1 + \cos\phi)/\sin\phi$. Thus, we obtain the size of the overlapped area as $-r^2(1 + \cos\phi)/\sin\phi$ for both $\pi < \phi \leq 3\pi/2$ and $3\pi/2 \leq \phi < 2\pi$. □

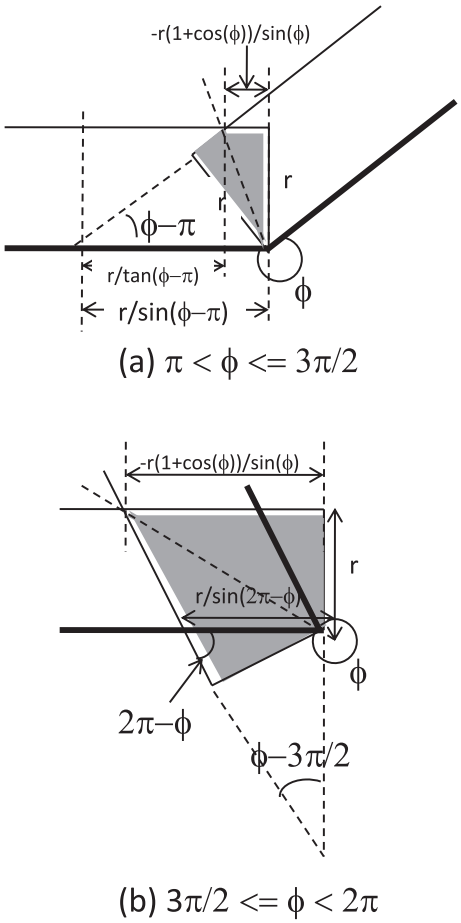

Fig. A· 9 Overlapped detectable area with disk-shaped sensing area.

B.3 Proof of Proposition

Note that the detectable area of the target object consists of the target object itself, the detectable rectangles associated with each boundary line segment, and the detectable circular-sector-shaped areas associated with each convex vertex. However, there may be some overlaps among them (Fig. A· 6). If a detectable rectangle or a detectable circular-sector-shaped area overlaps the target object itself, this means it also overlaps other detectable rectangles or detectable circular-sector-shaped areas. Thus, we focus on the possibility of overlaps among detectable rectangles and detectable circular-sector-shaped areas, i.e., the possibility of overlaps between (i) two detectable rectangles, (ii) two detectable circular-sector-shaped areas, and (iii) a detectable rectangle and a circular-sector-shaped area.

By using Lemma 1, we find that a non-zero size overlap for the detectable rectangle $\rho(r, L)$ can happen only with $\rho(r, L')$ where $L' \circ L$. That is, we can remove the possibility of (iii) mentioned above and need to consider the possibility of (i) with the condition $L' \circ L$ for two detectable rectangles $\rho(r, L)$ and $\rho(r, L')$. In addition, by using Lemma 2, we can remove the possibility of (ii).

We should note that the detectable area size is the sum of the target object size, the sizes of the detectable rectangles, and the sizes of the detectable circular-sector-shaped areas minus the sizes of the overlapping areas. We also note that $\|\mathcal{D}\| = \frac{1}{2\pi}\int_{\mathcal{D}} dxdyd\theta = \int_{\mathcal{D}} dxdy$ because the size of the detectable area for the disk-shaped sensing area is independent of θ. Thus, by using Lemma 3 and notations that a_i be the length of the i-th boundary line segment, ϕ_j be the j-th interior angle smaller than π, and $\hat{\phi}_k$ be the k-th interior angle larger than π ($i, j, k = 1, 2, \cdots$),

$$\begin{aligned}\|\mathcal{D}\| &= \|\mathcal{T}\| + \sum_i a_i r + \sum_j r^2(\pi - \phi_j)/2 \\ &\quad - \sum_k \{-r^2(1 + \cos\hat{\phi}_k)/\sin\hat{\phi}_k\} \\ &= \|\mathcal{T}\| + r|\mathcal{T}| + \alpha r^2, \end{aligned} \tag{A· 3}$$

where $\alpha = \sum_j(\pi - \phi_j)/2 + \sum_k(1 + \cos\hat{\phi}_k)/\sin\hat{\phi}_k$. □

Appendix C: Error Size

In the numerical example, the estimation error sizes (perimeter length estimation error size $\epsilon(|\mathcal{T}|)$, size estimation error size $\epsilon(\|\mathcal{T}\|)$, and α estimation error size $\epsilon(\alpha)$) were defined as follows. Based on Eqs. (10), (11), and (12),

$$\epsilon(|\mathcal{T}|) = 2\pi\Big(\tilde{v}_1(r_3^2 - r_2^2)^2 + \tilde{v}_2(r_1^2 - r_3^2)^2 + \tilde{v}_3(r_2^2 - r_1^2)^2\Big)^{1/2}/|C|, \quad (\mathrm{A}\cdot 4)$$

$$\epsilon(\|\mathcal{T}\|) = \Big(\tilde{v}_1(r_2^2|\mathcal{A}_3| - r_3^2|\mathcal{A}_2|)^2 + \tilde{v}_2(r_3^2|\mathcal{A}_1| - r_1^2|\mathcal{A}_3|)^2 + \tilde{v}_3(r_1^2|\mathcal{A}_2| - r_2^2|\mathcal{A}_1|)^2\Big)^{1/2}/|C|, \quad (\mathrm{A}\cdot 5)$$

$$\epsilon(\alpha) = \Big(\tilde{v}_1(|\mathcal{A}_2| - |\mathcal{A}_3|)^2 + \tilde{v}_2(|\mathcal{A}_3| - |\mathcal{A}_1|)^2 + \tilde{v}_3(|\mathcal{A}_1| - |\mathcal{A}_2|)^2\Big)^{1/2}/|C|, \quad (\mathrm{A}\cdot 6)$$

where $\tilde{v}_i = var_i/\lambda_i^2$ $(i = 1, 2, 3)$ (var_i are variations of the sample $\tilde{I}_i$). We used var_i measured in the simulation. These estimation error sizes are the standard deviations of the estimates under assumption of independence of $\tilde{I}_1$, $\tilde{I}_2$, and $\tilde{I}_3$ from each other.

Hiroshi Saito graduated from the University of Tokyo with a B.E. degree in Mathematical Engineering in 1981, an M.E. degree in Control Engineering in 1983 and received Dr.Eng. in Teletraffic Engineering in 1992. He joined NTT in 1983. He is currently an Executive Research Engineer at NTT Service Integration Labs. He received the Young Engineer Award of the Institute of Electronics, Information and Communication Engineers (IEICE) in 1990, the Telecommunication Advancement Institute Award in 1995 and 2010, and the excellent papers award of the Operations Research Society of Japan (ORSJ) in 1998. His research interests include traffic technologies of communications systems, network architecture, and ubiquitous systems. Dr. Saito is a fellow of IEEE, and ORSJ, and a member of IFIP WG 7.3.

Sadaharu Tanaka received the B.E. and M.E. degrees in communication system engineering from Chiba University, Japan, in 2008 and 2010, respectively. Currently, he is with the Yahoo Japan Corporation. His research interest includes the performance analysis of sensor networks.

Shigeo Shioda received the B.S. degree in physics from Waseda University in 1986, the M.S. degree in physics from University of Tokyo in 1988, and the Ph.D. degree in teletraffic engineering from University of Tokyo, Tokyo, Japan, in 1998. In 1988 he joined NTT, where he was engaged in research on measurements, dimensioning and controls for ATM-based networks. Since March 2001, he has been with the graduate school of engineering, Chiba University, Japan, where he is now Professor. His research interests are in the field of performance evaluation of wireless networks, P2P systems, queueing theory, and complex networks. Prof. Shioda is a member of the ACM, the IEEE, and the Operation Research Society of Japan.